nature portfolio

https://doi.org/10.1038/s41563-022-01294-2

Supplementary information

Directed cell migration towards softer environments

In the format provided by the authors and unedited

Supplementary information for:

Directed cell migration towards softer environments

Aleksi Isomursu[1,12], Keun-Young Park[2,12], Jay Hou[3,12], Bo Cheng[4,5,12], Mathilde Mathieu[1], Ghaidan A. Shamsan[3], Benjamin Fuller[3], Jesse Kasim[3], M. Mohsen Mahmoodi[2], Tian Jian Lu[6,7], Guy M. Genin[4,5,8], Feng Xu[4,5], Min Lin[4,5,*], Mark D. Distefano[2,*], Johanna Ivaska[1,9,10,11,*], and David J. Odde[3,*]

[1]Turku Bioscience Centre, University of Turku and Åbo Akademi University, Turku, Finland
[2]Department of Chemistry, University of Minnesota, Minneapolis, MN, USA
[3]Department of Biomedical Engineering, University of Minnesota, Minneapolis, MN, USA
[4]The Key Laboratory of Biomedical Information Engineering of Ministry of Education, School of Life Science and Technology, Xi'an Jiaotong University, Xi'an, P.R. China
[5]Bioinspired Engineering and Biomechanics Center (BEBC), Xi'an Jiaotong University, Xi'an, P.R. China
[6]State Key Laboratory of Mechanics and Control of Mechanical Structures, Nanjing University of Aeronautics and Astronautics, Nanjing, P.R. China
[7]MOE Key Laboratory of Multifunctional Materials and Structures, Xi'an Jiaotong University, Xi'an, P.R. China
[8]NSF Science and Technology Center for Engineering Mechanobiology, Washington University in St. Louis, St. Louis, MO, USA
[9]Department of Life Technologies, University of Turku, Turku, Finland
[10]InFlames Research Flagship Center, University of Turku, Turku, Finland
[11]Foundation for the Finnish Cancer Institute, Helsinki, Finland

[12]These authors have contributed equally to the work
*Correspondence to: minlin@xjtu.edu.cn (M.L.); diste001@umn.edu (M.D.D.); johanna.ivaska@utu.fi (J.I.); oddex002@umn.edu (D.J.O.)

This file includes:

- List of additional Source Data files
- Supplementary Figures 1–17
- Supplementary Notes 1–3
- Supplementary Tables 1–3
- Captions for Supplementary Videos 1–3
- Supplementary References
- List of additional Supplementary Data files

Source Data files related to the main Figures

- Source Data Fig. 1: statistical source data
- Source Data Fig. 2: unprocessed western blots
- Source Data Fig. 2: statistical source data
- Source Data Fig. 3: statistical source data
- Source Data Fig. 4: statistical source data
- Source Data Fig. 5: unprocessed western blots
- Source Data Fig. 5: statistical source data

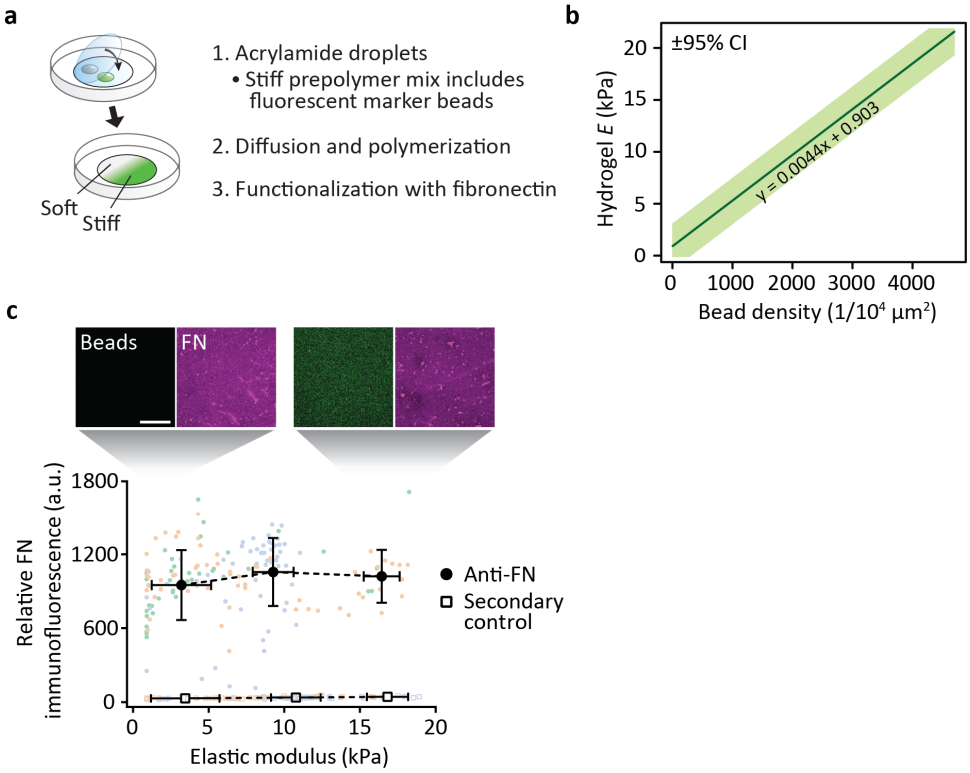

Supplementary Figure 1. Preparation of diffusion-based stiffness gradient hydrogels. (a) Schematic representation of stiffness gradient preparation. Two acrylamide solutions are polymerized and mixed together on a glass bottom dish to create a continuous gradient in the range of 0.5–22 kPa. The hydrogel is activated and functionalized with fibronectin before use. (b) Calibration curve connecting fluorescent marker bead density, measured using a confocal microscope, to the elastic modulus of the hydrogel. Adapted from Ref.[1] (c) Fibronectin density across the stiffness gradient hydrogels, measured via immunofluorescence. Green, orange and blue colors denote measurements from three individual experiments, overlaid with binned data. Squares depict measurements from secondary controls, stained by omitting the anti-fibronectin antibody. Scale bar, 50 µm. Mean ± SD of n = 86 (anti-FN, low), 54 (anti-FN, intermediate), 19 (anti-FN, high), 23 (control, low), 42 (control, intermediate) and 9 (control, high) regions of interest (ROI).

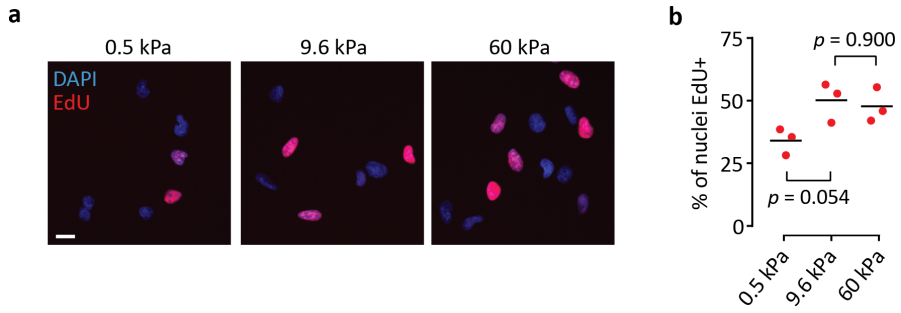

Supplementary Figure 2. Mechanosensitivity of U-251MG proliferation. (a–b) Fluorescence images (a) and quantification (b) depicting EdU incorporation by U-251MG cells on 0.5–60 kPa substrates. Scale bar, 20 µm. Mean values from three independent experiments. Analyzed by one-way ANOVA and Sidak's *post hoc* test.

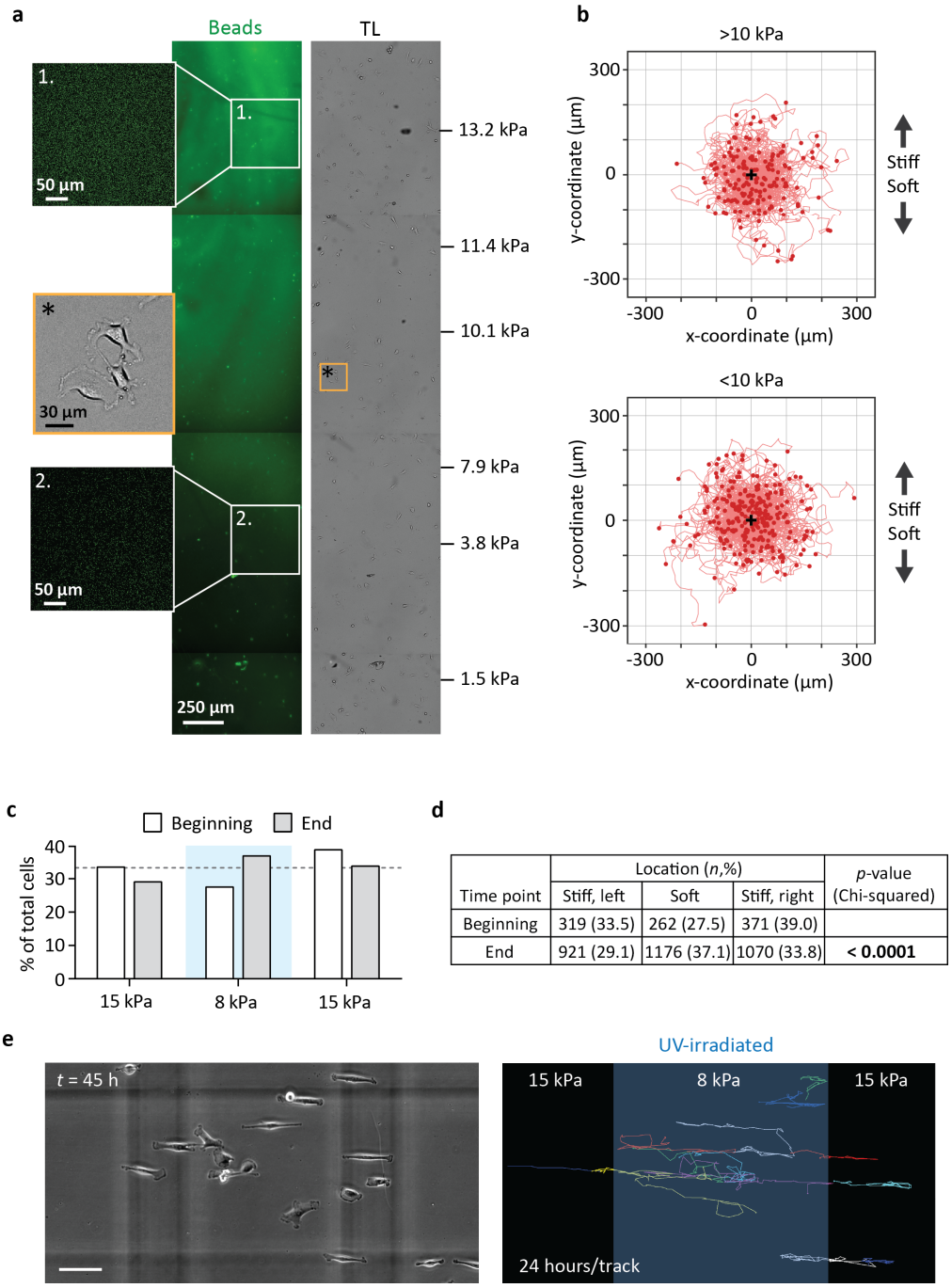

Time point	Location (*n*,%)			*p*-value (Chi-squared)
	Stiff, left	Soft	Stiff, right	
Beginning	319 (33.5)	262 (27.5)	371 (39.0)	
End	921 (29.1)	1176 (37.1)	1070 (33.8)	**< 0.0001**

Supplementary Figure 3. Tracking individual U-251MG cells on stiffness gradients. (a) Representative fluorescence image of a stiffness gradient hydrogel (left) and live U-251MG cells adhering to the substrate (right). Relates to the data in Fig. 1d. (Insets 1 and 2) Example confocal images of fluorescent beads, acquired as described in Ref.[1] The images correspond to the indicated gradient regions and were used for calculating the substrate elastic moduli. (*) Close up of the cells. (b) Tracks from individual U-251MG cells migrating on the stiffer (>10 kPa, top) and softer (<10 kPa, bottom) regions of a 0.5–22 kPa stiffness gradient for 10 hours. The tracks correspond to the data in Fig. 1d and the origo (0,0) is highlighted by a black '+'. *n* = 174 (>10 kPa) and 264 (<10 kPa) cells, from three independent experiments. (c–d) Total number of cells in the different gradient regions in Fig. 1f–g. (c) Bar graph, *n* = 952 (beginning) and 3,167 (end) cells per time point, from two individual experiments. (d) Contingency table summarizing the data, analyzed by chi-squared test (two-sided). (e) Endpoints (left) and 24-hour tracks (right) depicting the migration of individual cells on the photoresponsive stiffness gradients in Fig. 1f. Scale bar, 100 µm.

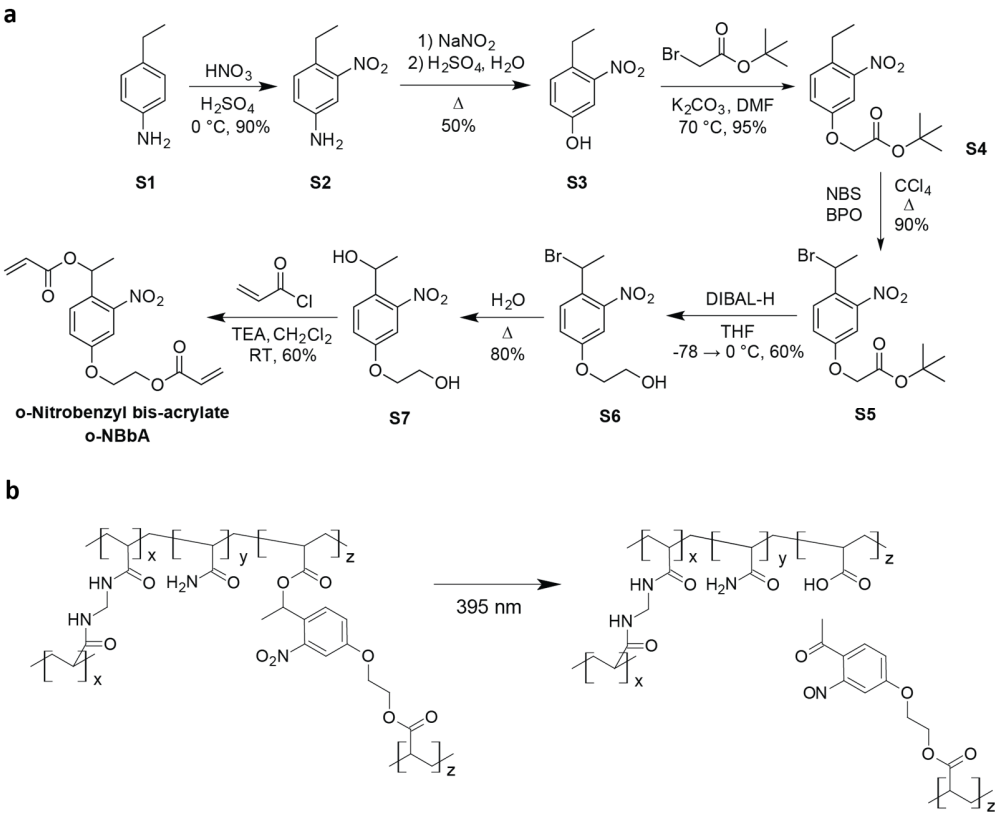

Supplementary Figure 4. Synthesis and photochemistry of o-nitrobenzyl bis-acrylate. (a) Schematic of the synthesis of o-NBbA. (b) Copolymerization of o-NBbA with acrylamide and bis-acrylamide yields hydrogels composed of strands of polyacrylamide crosslinked by either o-NBbA or bis-acrylamide. UV irradiation cleaves the photolabile o-NBbA, resulting in gels with lower crosslinking density and hence lower stiffness. The process does not release any byproducts to the gel environment.

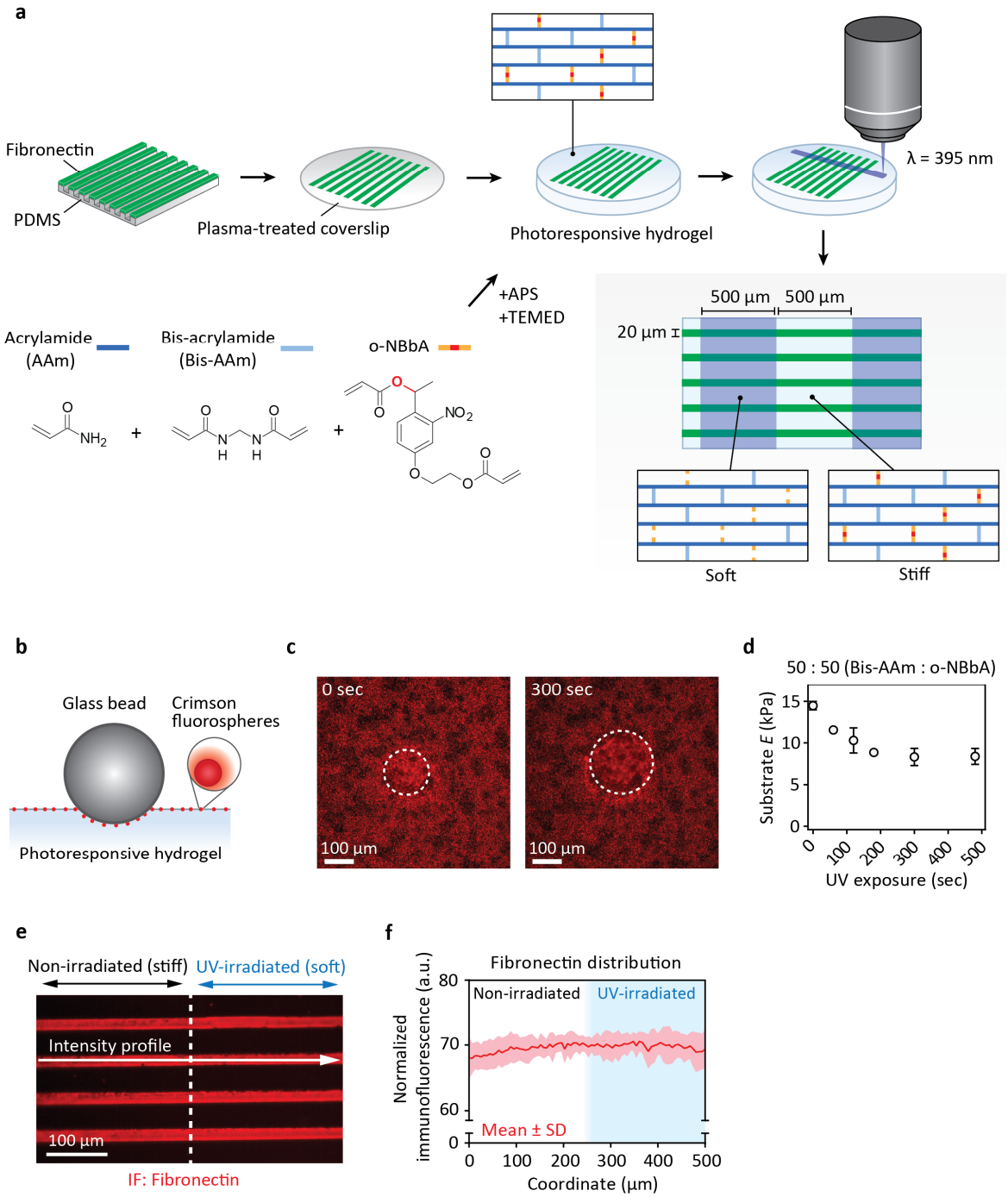

Supplementary Figure 5. Preparation and characterization of photoresponsive hydrogels. (a) Schematic representation of stiffness gradient preparation for migration experiments. The photocleavable carbon-oxygen bond in o-NBbA is indicated by red color. (b–d) Stiffness characterization by bead indentation. A schematic representation of the technique (b), representative fluorescence images (c) and quantified results (d) depicting hydrogel elasticity as a function of UV exposure. Dashed lines highlight indented, out-of-focus areas in the gel. Mean ± SD of $n = 3$ measurements. (e–f) Validation of the microcontact printed fibronectin patterns. Immunofluorescence image (e) and quantification (f) showing fibronectin distribution on non-irradiated and UV-exposed regions of the hydrogel. Mean ± SD of $n = 24$ intensity profiles.

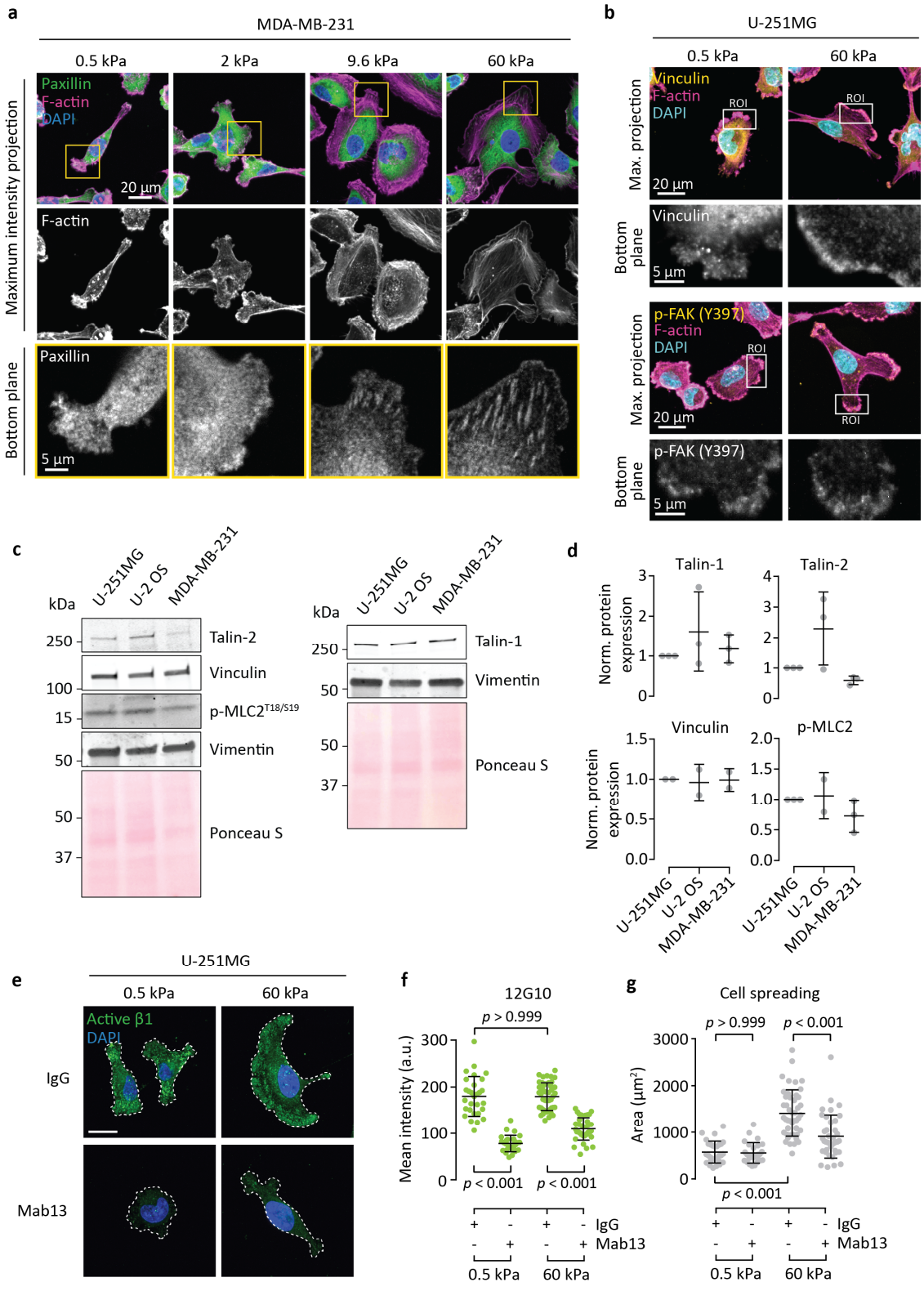
a
MDA-MB-231
0.5 kPa
2 kPa
9.6 kPa
60 kPa
Maximum intensity projection
Paxillin
F-actin
DAPI
20 µm
F-actin
Bottom plane
Paxillin
5 µm
b
U-251MG
0.5 kPa
60 kPa
Max. projection
Vinculin
F-actin
DAPI
ROI
20 µm
Bottom plane
Vinculin
5 µm
p-FAK (Y397)
F-actin
DAPI
ROI
20 µm
Bottom plane
p-FAK (Y397)
5 µm
c
kDa
U-251MG
U-2 OS
MDA-MB-231
250
Talin-2
Vinculin
100
15
p-MLC2T18/S19
Vimentin
50
50
Ponceau S
37
kDa
U-251MG
U-2 OS
MDA-MB-231
250
Talin-1
Vimentin
50
50
Ponceau S
37
d
Talin-1
Talin-2
Norm. protein expression
Vinculin
p-MLC2
Norm. protein expression
U-251MG
U-2 OS
MDA-MB-231
e
U-251MG
0.5 kPa
60 kPa
Active β1
DAPI
IgG
Mab13
f
12G10
p > 0.999
Mean intensity (a.u.)
p < 0.001
p < 0.001
IgG
Mab13
0.5 kPa
60 kPa
g
Cell spreading
p > 0.999
p < 0.001
Area (µm²)
p < 0.001
IgG
Mab13
0.5 kPa
60 kPa

Supplementary Figure 6. Focal adhesion maturation and adhesion components in U-251MG and other cancer cells. (a) Immunofluorescence images of paxillin and F-actin in MDA-MB-231 cells on 0.5–60 kPa substrates. The bottom panels show individual focal planes from confocal stacks, corresponding to the basal side of each cell. Scale bar, 20 µm. Representative of two independent experiments. (b) Immunofluorescence images of vinculin (top), p-FAK (bottom) and F-actin in U-251MG cells on 0.5 and 60 kPa substrates. The bottom panels show individual focal planes from confocal stacks, corresponding to the basal side of each cell. Representative of one (vinculin) to two (p-FAK) independent experiments. (c–d) Representative western blots (c) and quantification (d) depicting talin-1/2, vinculin and p-MLC2 levels across three different cell lines. Densitometric measurements were normalized to vimentin, mean ± SD of n = 2 (vinculin; p-MLC2: U-2 OS) or 3 (talin-1; talin-2; p-MLC2: U-251MG, MDA-MB-231) independent experiments. (e–f) Immunofluorescence images (e) and quantification (f) showing active β1-integrin (clone 12G10) in U-251MGs on 0.5 and 60 kPa substrates. The cells were treated with a control antibody (normal rat IgG) or β1 function-blocking Mab13 for two hours before fixation. Scale bar, 20 µm. Mean ± SD of n = 29 (0.5 kPa, IgG), 27 (0.5 kPa, Mab13), 45 (60 kPa, IgG) and 39 (60 kPa, Mab13) cells, analyzed by Kruskal-Wallis one-way ANOVA and Dunn's *post hoc* test. Representative of two independent experiments. (g) Spreading of U-251MGs on 0.5 and 60 kPa substrates, without or after β1-integrin blocking by Mab13. Mean ± SD of n = 29 (0.5 kPa, IgG), 27 (0.5 kPa, Mab13), 45 (60 kPa, IgG) and 39 (60 kPa, Mab13) cells, analyzed by Kruskal-Wallis one-way ANOVA and Dunn's *post hoc* test. Representative of two independent experiments.

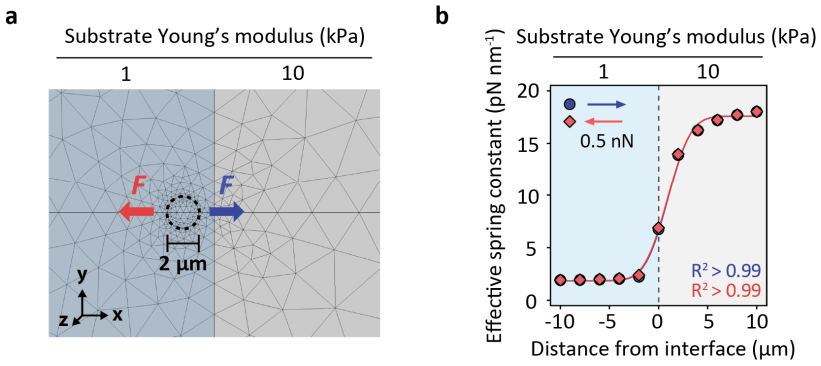

Supplementary Figure 7. Finite element analysis of polyacrylamide displacement next to a stepwise elastic gradient. (a) COMSOL Multiphysics® model setup. (b) The effect of steep elastic gradients on the effective spring constant of polyacrylamide. A lateral 0.5 nN force was exerted on the substrate through a circular adhesion zone (r = 1 µm) as shown in (a). The position of the adhesion zone was adjusted repeatedly at 2 µm steps. The direction of the force was varied by 180° but was always parallel to the gradient. In both cases, normal cumulative distribution function was a good fit to the data.

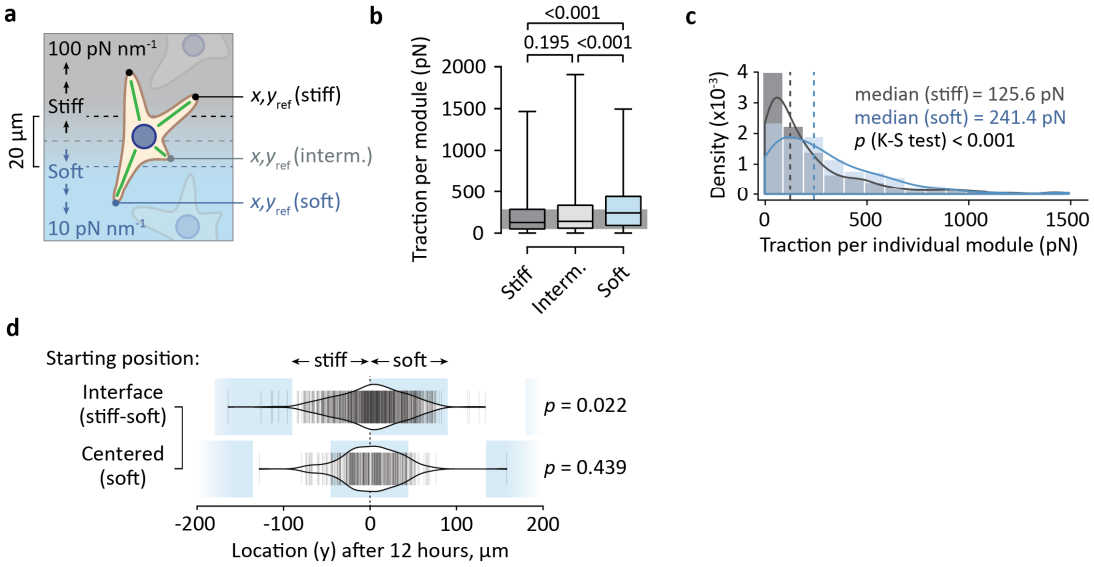

Supplementary Figure 8. CMS produces asymmetric traction forces in cells that interact with stiffness gradients. (a) When individual cells were on top of a stiffness gradient during the simulations in Fig. 3b–f, their traction forces were recorded. (b–c) Forces exerted by clutch modules on stiff, intermediate and soft substrate, when the cell body is located on a stiffness gradient. (b) Box plot depicting mean traction per module for n = 365 (stiff), n = 1380 (intermediate) and n = 292 (soft) modules. Each box displays upper and lower quartiles and a median, the whiskers denote minimum and maximum values. Analyzed by Kruskal-Wallis one-way ANOVA and Dunn's *post hoc* test, p-values are indicated in the figure. (c) Histograms overlaid with probability density functions, dashed lines indicate medians. n = 292 (soft) and 365 (stiff) modules, analyzed by Kolmogorov-Smirnov test (two-sided). (d) Violin plots of accumulated distance migrated by individual cells along the orientation of the gradient and over 12 hours, starting from a gradient (top) or from the middle of a compliant region (bottom). n = 326 (soft) and 759 (interface) cells, analyzed by sign test (two-sided).

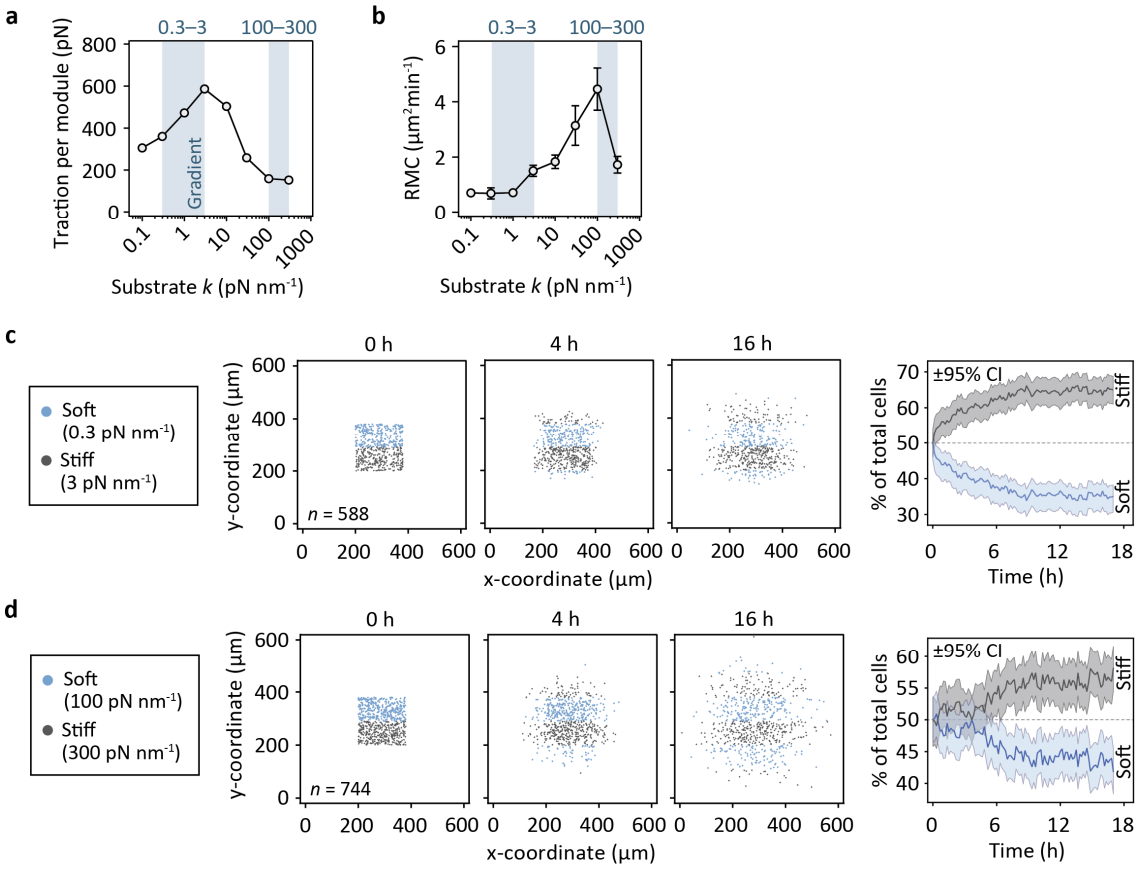

Supplementary Figure 9. Modifying the range of the stiffness gradient can reverse durotaxis *in silico*. (a–b) Module traction forces (a) and RMC (b) of the simulated cells as a function of substrate stiffness, as in Fig. 3c–d. Overlays highlight the ranges of the 0.3–3 pN nm^{-1} and 100–300 pN nm^{-1} gradients in (c–d). Mean ± SEM of n = 10 cells. (c–d) Evolution of cell density on mechanically heterogeneous substrates over time. (c) Coordinates of individual cells on the 0.3–3 pN nm^{-1} gradient 0, 4 and 16 hours into the simulation (left) and the fraction of cells residing in the stiffer and softer areas over the course of the simulation (right). ±95% CI, n = 588 cells. (d) As above, but for the 100–300 pN nm^{-1} gradient. n = 744 cells.

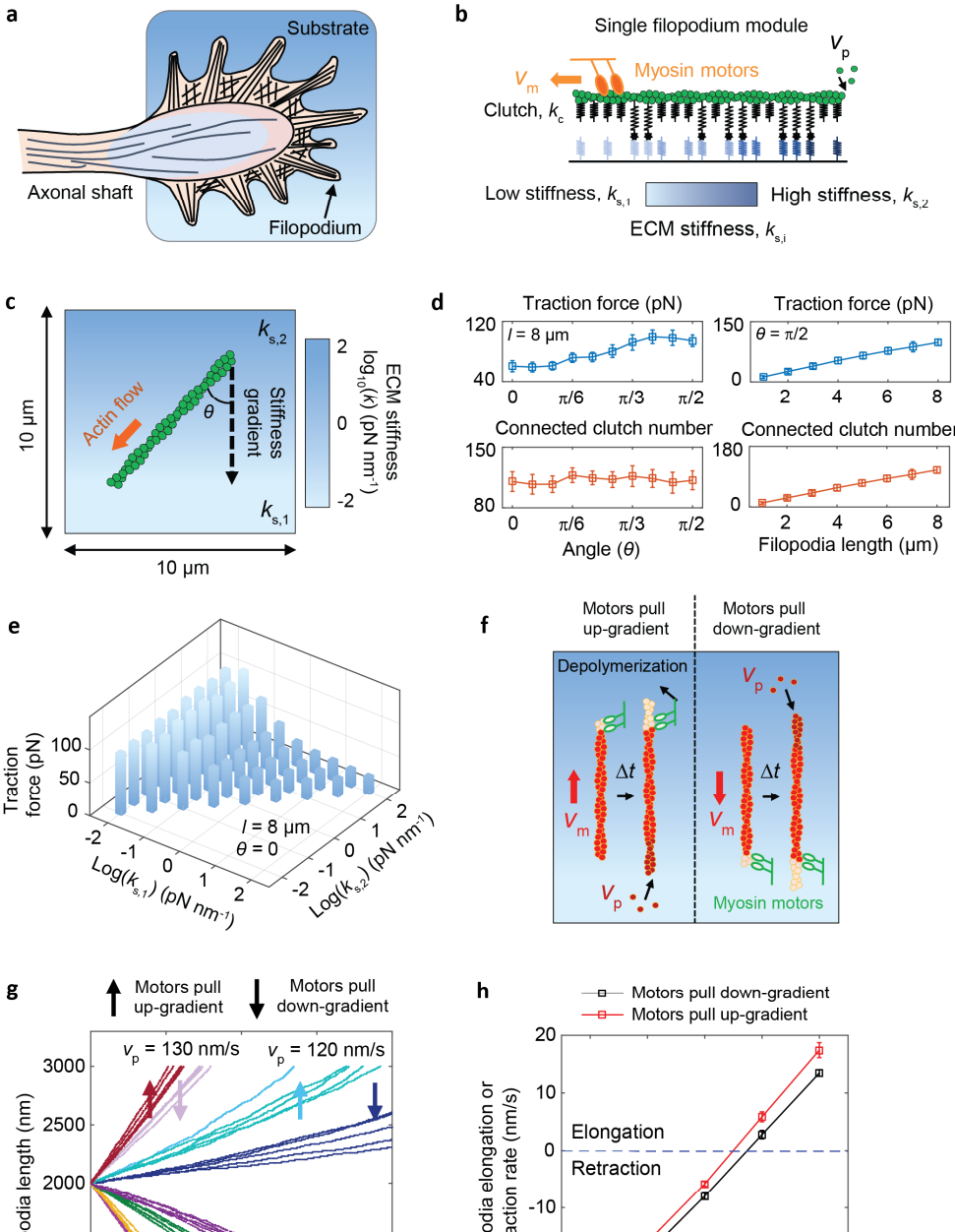
a
Substrate
Axonal shaft
Filopodium
b
Single filopodium module
V_p
V_m
Myosin motors
Clutch, k_c
Low stiffness, $k_{s,1}$
High stiffness, $k_{s,2}$
ECM stiffness, $k_{s,i}$
c
$k_{s,2}$
Actin flow
Stiffness gradient
θ
$k_{s,1}$
10 μm
10 μm
2
0
-2
ECM stiffness $\log_{10}(k)$ (pN nm^{-1})
d
Traction force (pN)
l = 8 μm
Traction force (pN)
θ = π/2
Connected clutch number
Connected clutch number
Angle (θ)
Filopodia length (μm)
e
Traction force (pN)
l = 8 μm
θ = 0
Log($k_{s,1}$) (pN nm^{-1})
Log($k_{s,2}$) (pN nm^{-1})
f
Motors pull up-gradient
Motors pull down-gradient
Depolymerization
V_p
Δt
V_m
Myosin motors
g
Motors pull up-gradient
Motors pull down-gradient
v_p = 130 nm/s
v_p = 120 nm/s
v_p = 100 nm/s
v_p = 110 nm/s
Filopodia length (nm)
Time (s)
h
Motors pull down-gradient
Motors pull up-gradient
Elongation
Retraction
Filopodia elongation or retraction rate (nm/s)
Actin polymerization rate (nm/s)

Supplementary Figure 10. Motor-clutch model of filopodial dynamics. (a) Schematic representation of a neuronal GC. Filopodia, surrounded by a less polarized actin network, reside in the peripheral domain. They are separated from the axon by a thin transitional domain, and a central domain (light blue) that is primarily composed of microtubules. (b) The filopodia in GCs are modeled as individual motor-clutch modules, with adhesion springs (homogeneous stiffness), substrate springs (heterogeneous stiffness) and inward actin flow resulting from active myosin motors. Actin monomers are added into the filaments at a constant rate. (c) Setup used in the single-filopodium simulations. The filopodium interacts with the substrate in a set orientation relative to the linear stiffness gradient. (d) (Left) Traction force exerted by the filopodium increases when the protrusion is pointing down the gradient, toward softer substrate. (Right) Perpendicular to the gradient, traction increases with filopodia length mainly due to more clutches being available to bind with the substrate. Data shown are from n = 10 independent simulations. (e) Average traction exerted by a single filopodium on different substrate stiffness gradients. Data represent means of n = 10 simulations. (f) Filopodia length is affected by both actin flow, v_m, and the polymerization rate, v_p. Depending on the orientation of the filopodium, the actin may flow toward soft (filopodium pointing up the gradient) or stiff (filopodium pointing down the gradient) substrate. (g) Evolution of filopodia length on stiffness gradients upon different actin polymerization rates. The different combinations of v_p and filopodia orientation are color-coded, while each line represents the temporal variation in the length of a single filopodium. (h) Effect of actin polymerization and orientation relative to a stiffness gradient on the filopodia elongation/retraction rate. Data shown are from n = 10 independent simulations. Mean ± SEM in (d) and (h).

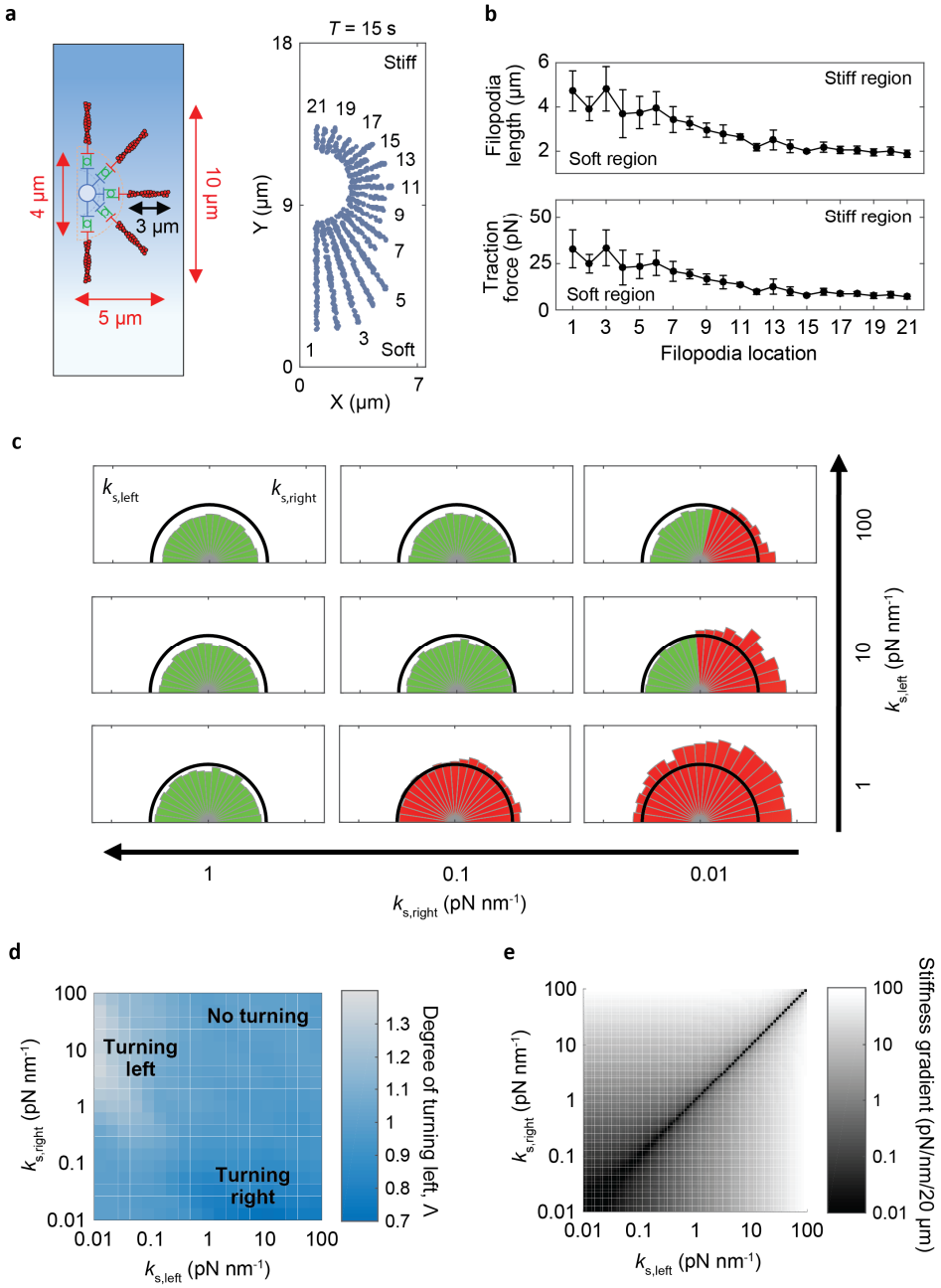

Supplementary Figure 11. Motor-clutch model predicts GC steering toward soft matrix. (a) Schematic representation of the GC model. (Left) Dimensions of a newly initialized GC. (Right) Each GC consists of multiple filopodia, distributed between –π/2 and π/2 relative to the axon. On stiffness gradients ($k_{s,1}$ = 0.01 pN nm^{-1}, $k_{s,2}$ = 100 pN nm^{-1}), filopodia on the more compliant side of the substrate rapidly outgrow the others, leading to effective turning of the GC. (b) Filopodia length (top) and traction (bottom) based on their orientation around the GC central domain. On stiffness gradients, filopodia pointing toward the softer substrate elongate faster and generate more traction. Mean ± SEM from n = 10 independent simulations. (c) Examples of GC behavior on different stiffness gradients. Green denotes filopodia that are retracting during the course of the simulation, red denotes filopodia that are elongating. Depending on the gradient, individual GCs may retract or enlarge isotropically, or steer toward the softer substrate. Displayed are means of n = 10 simulations. (d) Phase diagram of GC turning to left, Λ, on different mechanically graded substrates. (e) Phase diagram depicting the strength of the stiffness gradient for varying $k_{s,left}$ and $k_{s,right}$. Gradient strength alone cannot explain the magnitude of Λ, if the whole substrate is stiffer than the optimal range for individual filopodia (Supplementary Fig. 10e).

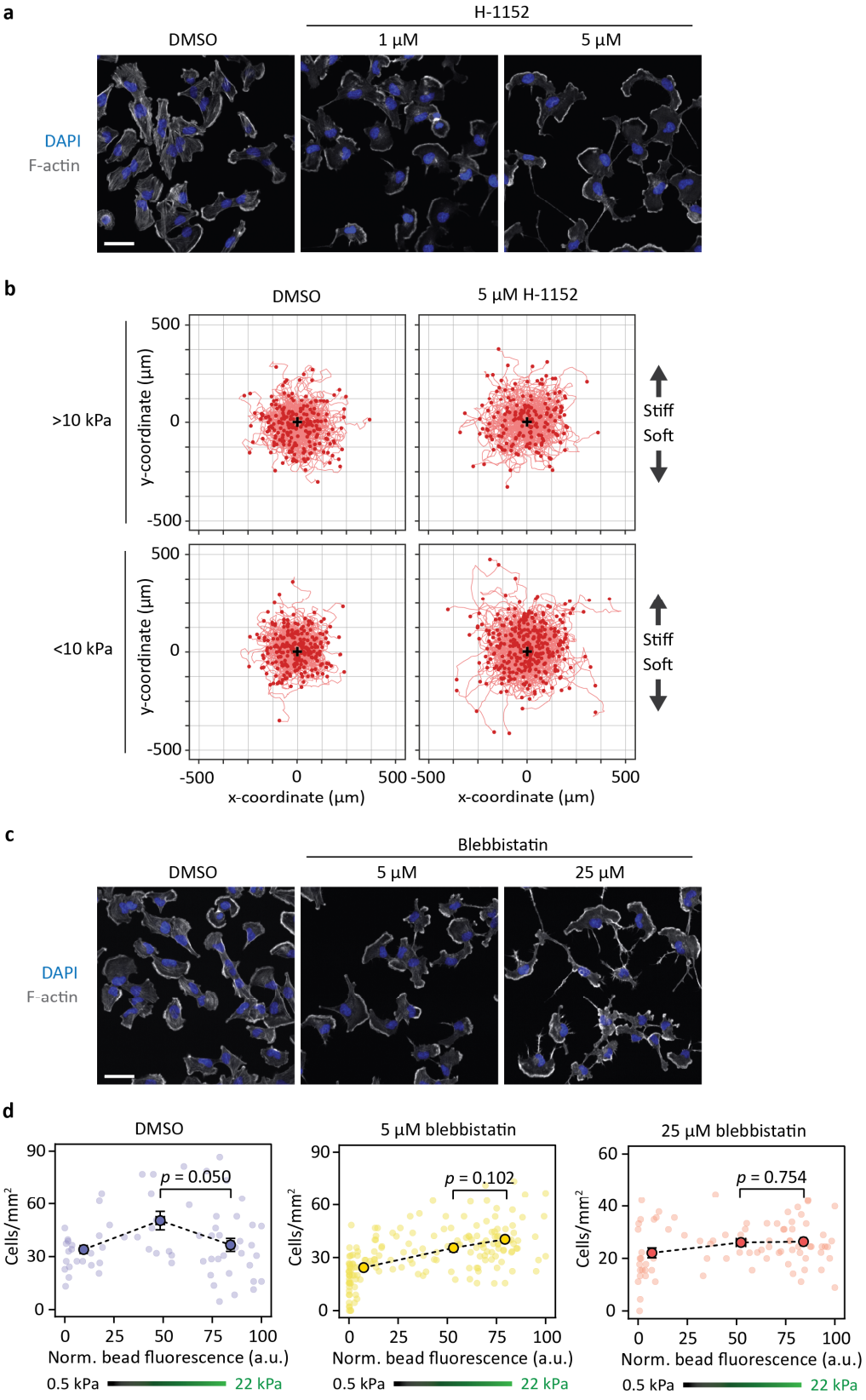
a
H-1152
DMSO
1 μM
5 μM
DAPI
F-actin
b
DMSO
5 μM H-1152
>10 kPa
<10 kPa
y-coordinate (μm)
x-coordinate (μm)
500
0
-500
Stiff
Soft
c
Blebbistatin
DMSO
5 μM
25 μM
DAPI
F-actin
d
DMSO
5 μM blebbistatin
25 μM blebbistatin
p = 0.050
p = 0.102
p = 0.754
Cells/mm²
Norm. bead fluorescence (a.u.)
0.5 kPa
22 kPa

Supplementary Figure 12. Morphology and migration of U-251MG cells during ROCK and myosin II inhibition. (a) Effect of ROCK inhibition by H-1152 on the actin cytoskeleton of U-251MG cells. Fluorescence images of F-actin after treatment with intermediate and high doses of the compound for two hours. Scale bar, 50 µm. Representative of two independent experiments. (b) Tracks from individual U-251MG cells migrating on the stiffer (>10 kPa, top) and softer (<10 kPa, bottom) regions of a 0.5–22 kPa stiffness gradient for 10 hours, treated with 5 µM H-1152 or vehicle (DMSO). The tracks correspond to the data in Fig. 4g and each origo (0,0) is highlighted by a black '+'. *n* = 204 (DMSO, >10 kPa), 238 (DMSO, <10 kPa), 177 (H-1152, >10 kPa) and 327 (H-1152, <10 kPa) cells per condition, from one (DMSO) to two (H-1152) independent experiments. (c) Effect of myosin II inhibition by blebbistatin on the actin cytoskeleton of U-251MG cells. Fluorescence images of F-actin after treatment with intermediate and high doses of the compound for two hours. Scale bar, 50 µm. Representative of two independent experiments. (d) Cell densities in different parts of 0.5–22 kPa gradients, 48 hours after being seeded and supplemented with varying concentrations of blebbistatin. Mean ± SEM of *n* = 25 (DMSO, low), 13 (DMSO, intermediate), 30 (DMSO, high), 85 (5 µM blebbistatin, low), 38 (5 µM blebbistatin, intermediate), 53 (5 µM blebbistatin, high), 30 (25 µM blebbistatin, low), 18 (25 µM blebbistatin, intermediate) and 36 (25 µM blebbistatin, high) ROIs per bin, from two gradient hydrogels per condition, representative of two independent experiments. Analyzed by Mann-Whitney test (two-sided).

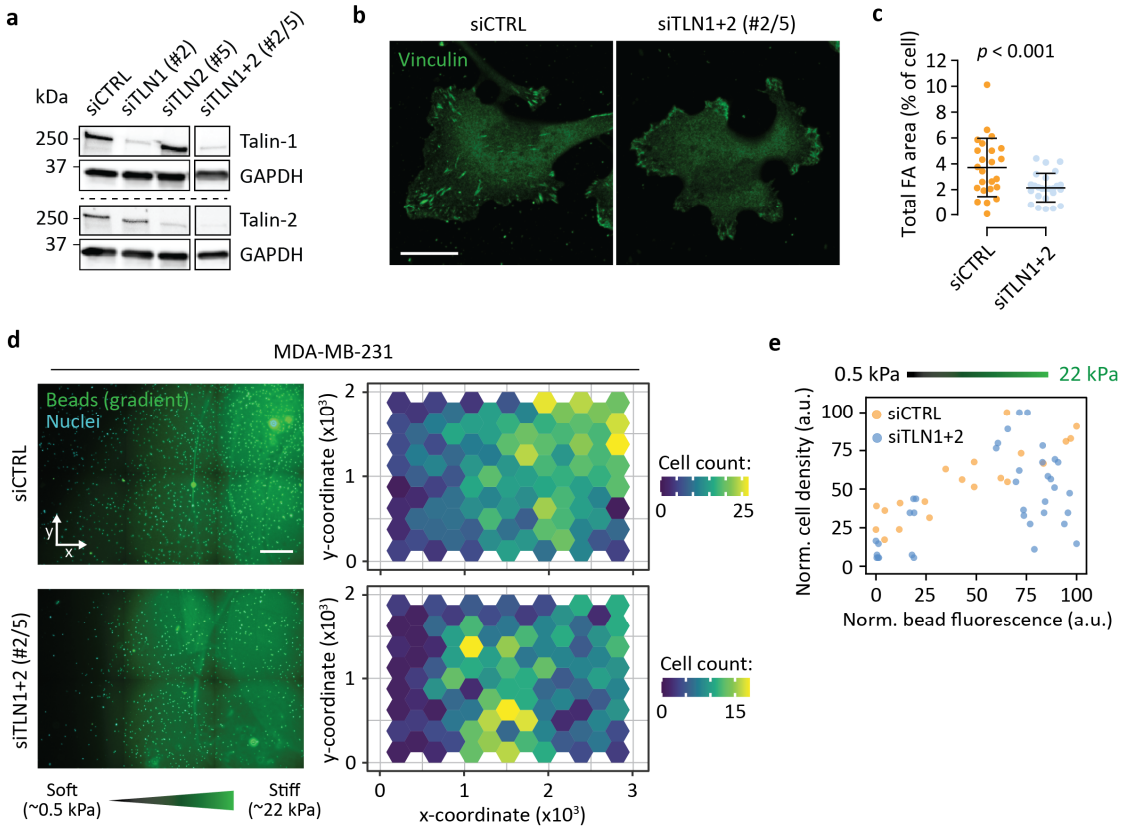

Supplementary Figure 13. Additional talin-1/2-targeting siRNAs recapitulate the loss of mature adhesions and promote a switch from positive to negative durotaxis in MDA-MB-231 cells. (a) Western blot depicting talin-1 and talin-2 knockdown in MDA-MB-231 cells using siRNA oligos that are different from the ones used in Fig. 5. The fourth band on each row, depicting a double knockdown, was cropped from a different site in the same membrane. Representative of two independent experiments. (b–c) Immunofluorescence images (b) and quantification (c) of vinculin-positive focal adhesions in MDA-MB-231s on 60 kPa substrate, without and after talin knockdown. Scale bar, 20 µm. Mean ± SD of n = 24 (siCTRL) and 25 (siTLN1+2) cells, analyzed by Mann-Whitney test (two-sided). Representative of two independent experiments. (d) (Left) Representative regions of two 0.5–22 kPa polyacrylamide stiffness gradients, 72 hours after being seeded with MDA-MB-231 cells. Scale bar, 500 µm. (Right) Quantification of cells across the gradients. (e) Relative MDA-MB-231 cell densities in different parts of the stiffness gradients. n = 20 (siCTRL) and 36 (siTLN1+2) ROIs, representative of two independent experiments.

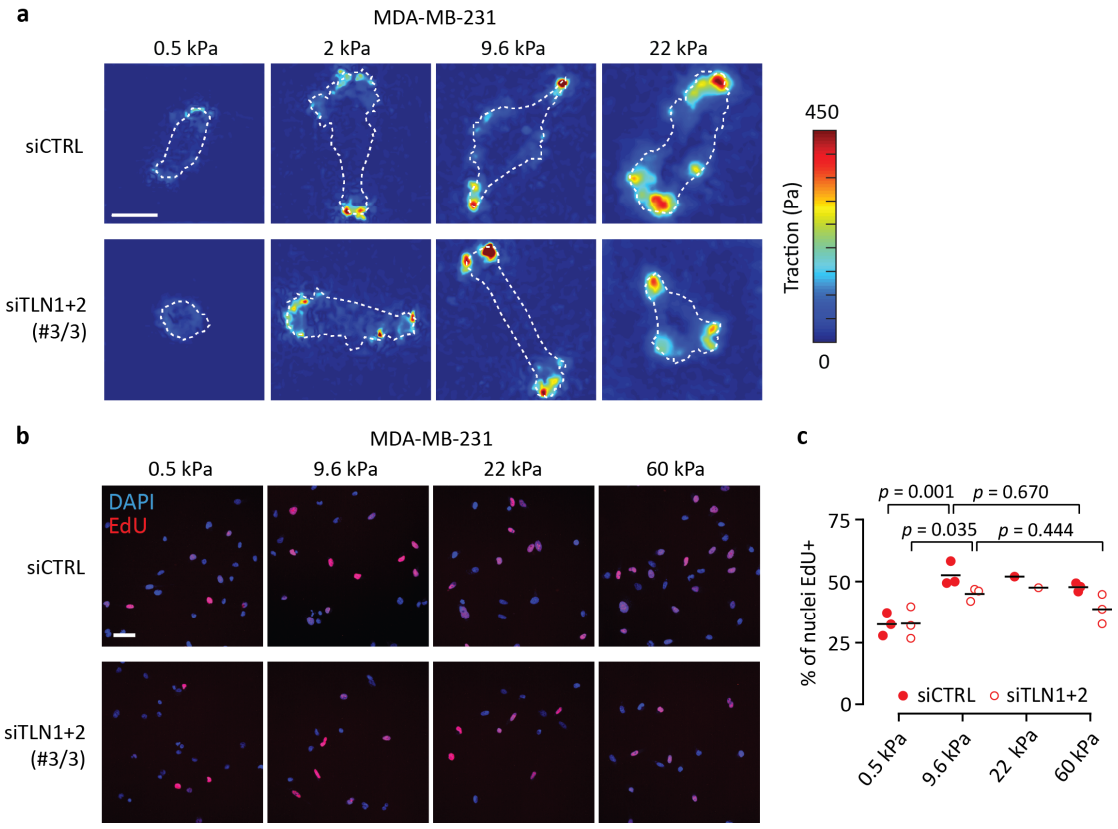

Supplementary Figure 14. Mechanosensitive traction and proliferation of MDA-MB-231 cells. (a) Representative traction maps from MDA-MB-231 cells on 0.5–22 kPa substrates, corresponding to the data from three independent experiments in Fig. 5f–h. Cell outlines are indicated by white dashed lines. Scale bar, 20 µm. (b–c) Fluorescence images (b) and quantification (c) depicting EdU incorporation by control and talin-low MDA-MB-231 cells on 0.5–60 kPa substrates. Scale bar, 50 µm. Mean values from *n* = 1 (22 kPa) or 3 (0.5 kPa, 9.6 kPa, 60 kPa) independent experiments. Analyzed by one-way ANOVA and Sidak's *post hoc* test.

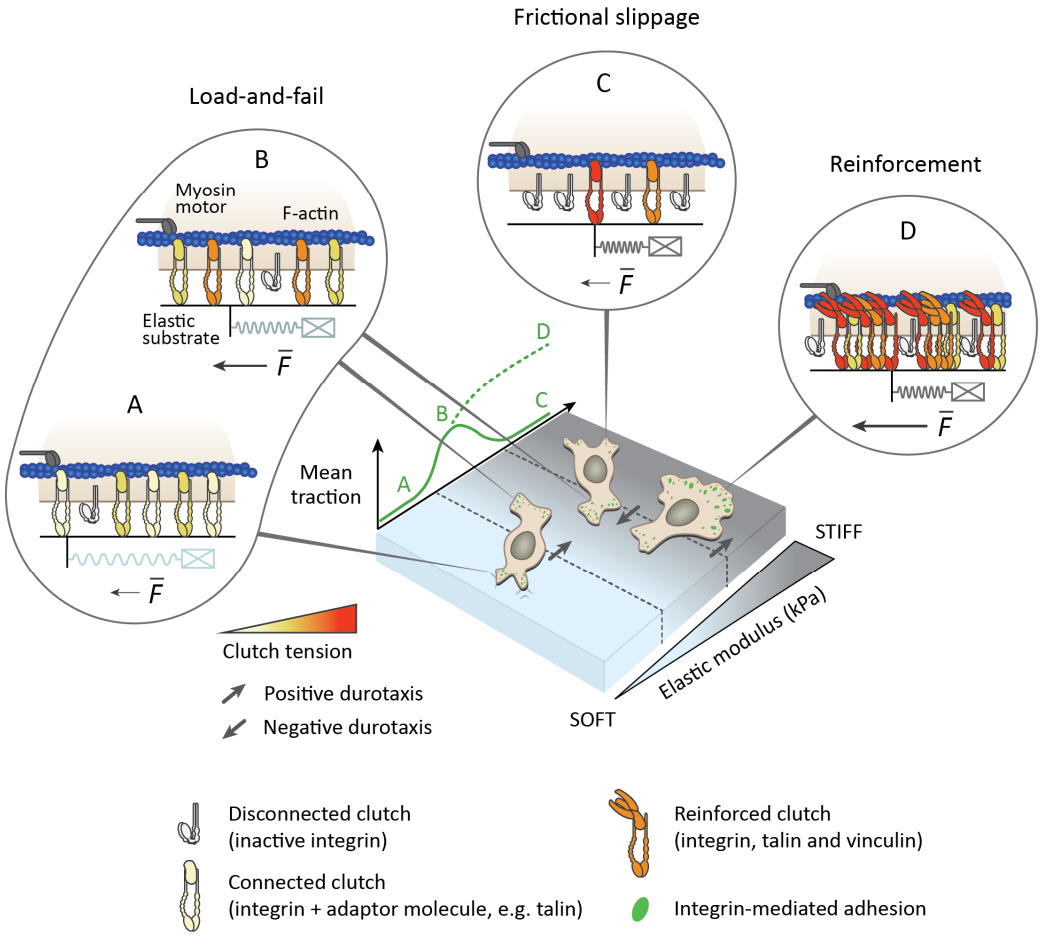

Supplementary Figure 15. Schematic representation of the regulation of positive and negative durotaxis by motor-clutch dynamics. Cell-intrinsic molecular machinery dictates the cell's capacity to exert force on mechanically heterogeneous substrates, driving positive or negative durotaxis. Without clutch reinforcement (mechanosensitive FA formation, D), the motor-clutch model predicts a biphasic relationship between traction force and substrate stiffness (A–C)[2–8]. This fundamental relationship, and the physical reinforcement of cell-matrix adhesion by FAs, are likely to be further influenced by biochemical signaling pathways and feedback loops that modulate the expression, activity and localization of individual cytoskeletal and clutch components, in a cell type-dependent manner.

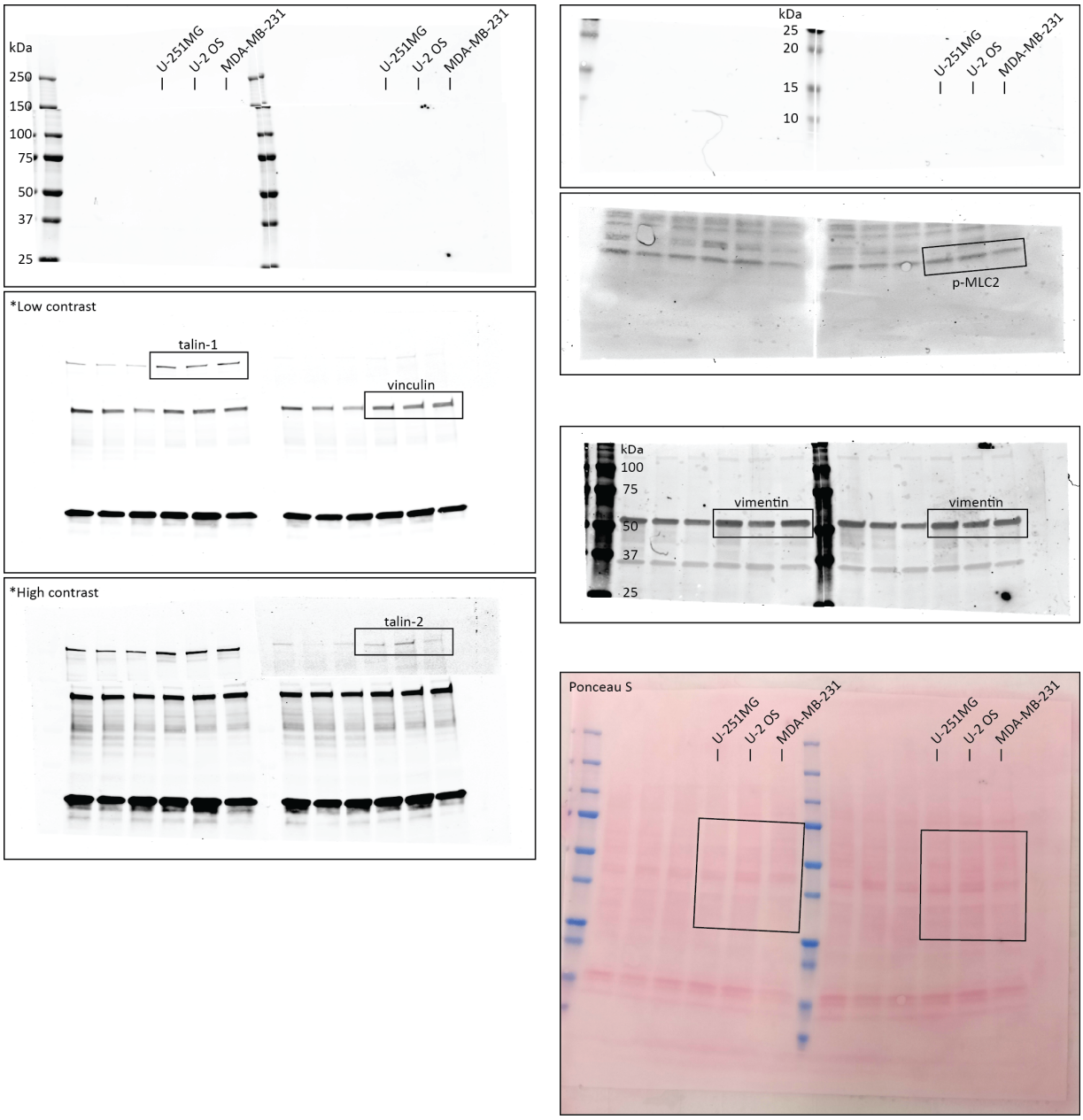

Supplementary Figure 16. Unprocessed western blot relating to Supplementary Fig. 6c.

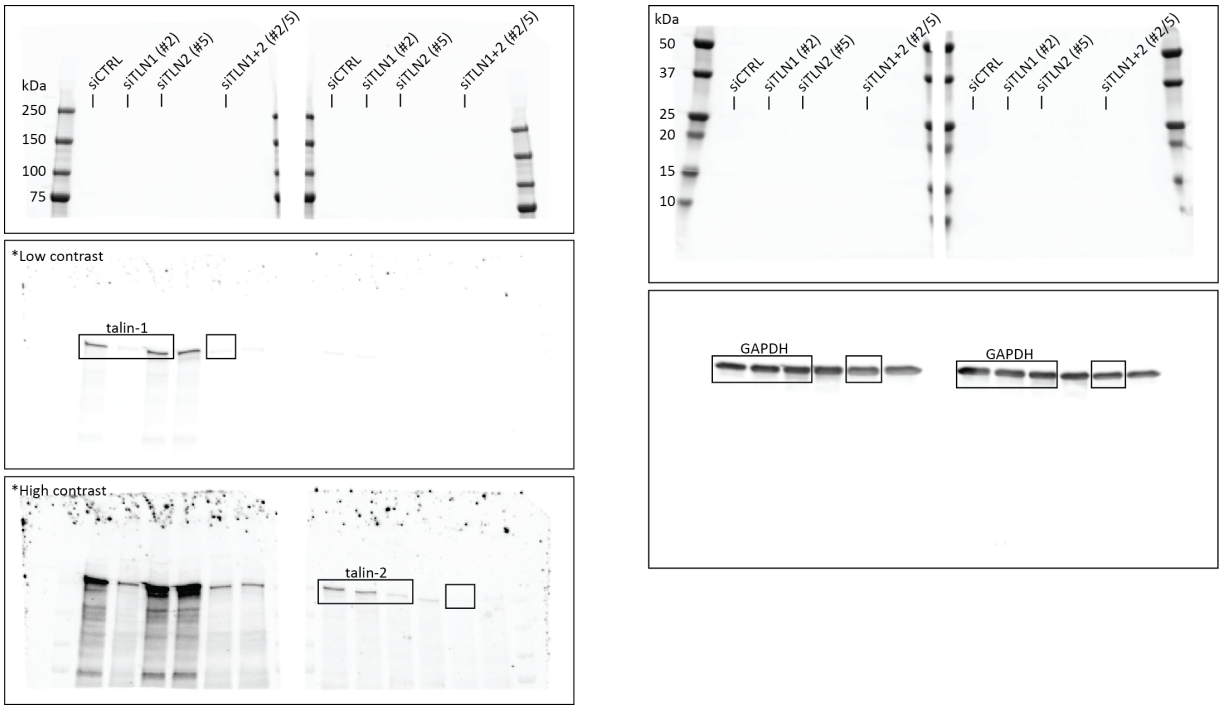

Supplementary Figure 17. Unprocessed western blot relating to Supplementary Fig. 13a.

Supplementary Note 1: Chemistry of o-NBbA and photoresponsive polyacrylamide hydrogels

Polyacrylamide was selected as the base material for the stiffness gradients used in this study, as it is the most widely employed model system for investigating the role of substrate stiffness in directing cell behavior. This is partly due to the ease of obtaining elastic moduli in a wide, physiologically relevant range[9,10]. While other types of gels (e.g. collagen or hyaluronic acid) are known to interact directly with cell surface receptors, including integrins, polyacrylamide gels are inert to such interactions. This allows more control over the types and densities of ligands that will be presented to the cells, making the material ideal for mechanobiological studies. Various methods have been developed to fabricate stiffness gradients in gels to study the durotactic behavior of cells. Some examples exploit the diffusion of two prepolymer solutions[1,11], tilted-superposition of two hydrogels[12], freeze-thaw-induced crosslinking of polyvinyl alcohol[13], or toehold-mediated strand displacement of DNA[14]. Aiming for high-resolution spatiotemporal control over the mechanical properties of the gel, we chose light as the external stimulus[15–19]. Therefore, we aimed to design and synthesize a new, minimalistic and photocleavable crosslinker that contains acrylate moieties.

Among various photolabile functionalities that are available, o-nitrobenzyl (o-NB) was chosen due to its high one-photon photolysis efficiency and high deprotection yields[20,21]. o-NB based compounds have been used widely in hydrogel-based studies to achieve controlled release or immobilization of payloads[22–26], photodegradation of gels[27–29], or modulation of gel stiffness[17,30]. However, many of these studies have focused on polyethylene glycol-based gels rather than polyacrylamide, or complete degradation of the gel rather than controlling the Young's modulus. To our knowledge, there has been only one report to date where o-NB-based crosslinkers have been used to fabricate photoresponsive polyacrylamide hydrogels[31]. While the study demonstrates the feasibility of o-NB based crosslinking, the method itself requires multiple steps to crosslink chains of polyacrylamide through the o-NB moiety, which made its application here unwieldy.

In this study, a simple one-step synthesis of photoresponsive polyacrylamide gels was enabled by the functionalization of an o-NB group with two acrylate moieties to yield a crosslinker that would cleave upon photolysis. The photocleavable crosslinker, o-nitrobenzyl bis-acrylate (o-NBbA), was synthesized in seven steps from p-ethyl aniline (Supplementary Fig. 4a) and designed so that its cleavage would not release any byproducts in the medium (Supplementary Fig. 4b). Based on a previously reported polyacrylamide recipe[32], a photoresponsive gel with an initial stiffness of 20 kPa that can be reduced down to 10 kPa was designed by replacing 50 mol % of bis-acrylamide with o-NBbA. The resulting gel exhibited a Young's modulus of ~15 kPa that was reduced down to ~8 kPa after complete cleavage of the o-NBbA crosslinker by exposure to 395

nm light for 5 min (Supplementary Fig. 5b–d). The slight discrepancy between the expected and measured substrate stiffness could be due to the relatively low water solubility and partial phase separation of o-NBbA in the prepolymer solution, which would result in softening of the hydrogel post-polymerization[33].

The light source used for the photocleavage was an LED from a SpectraX light engine instrument installed in a Nikon TiE microscope, originally intended for epifluorescence imaging. This method had several advantages: spatial control can be achieved easily, as the location of the substrate can be precisely chosen via phase-contrast imaging and the area of irradiation can be controlled with the field diaphragm and objectives. For instance, the diameter of the LED-irradiated area could be adjusted to as low as 59 µm using a 40x objective with a nearly closed field diaphragm, or as high as 978 µm under a 10x objective with a fully opened field diaphragm. Stiffness patterns could also be created using the 'time lapse movie' function of the NIS-Elements software (Nikon). Here, alternating stiffness gradients were created by initiating a time-lapse movie between two regions of the gel, a method that could be modified to yield more complex 1D patterns or even 2D shapes. Although not explored here, temporal control would be equally possible: for example, stiffness gradients could be introduced in gels at various time points during live cell culture, while simultaneously observing cellular behavior and responses.

To conjugate fibronectin to the surface of the gel via covalent interaction, acrylic acid N-hydroxysuccinimide (NHS) ester was used as the tethering agent. While two methods, addition of acrylic acid NHS ester in the pregel solution followed by stamping of fibronectin, or stamping of the pregel solution with fibronectin preincubated with acrylic acid NHS ester, both produced fibronectin-patterned hydrogels, the former was chosen since it yielded more consistent results. Once the gel had been fabricated, any remaining NHS ester moieties in the gel were passivated with bovine serum albumin (BSA) in PBS to prevent any non-specific interactions between the gel and cells.

Supplementary Note 2: Implementation of the cell migration simulator using mechanically heterogeneous substrates

To establish whether our observations of negative (and positive) durotaxis could be explained through a single set of principles, namely the motor-clutch dynamics of cell-matrix adhesions, we developed a modified version of the cell migration simulator (CMS) that can be used for modeling cell migration on mechanically heterogeneous substrates. The detailed governing equations and algorithms of the original CMS were described previously[7]. Briefly, the CMS comprises multiple motor-clutch models (i.e. modules) that mimic cellular protrusions found in U-251MG glioblastoma cells over the stiffness range used in the study. These include multiple lamellipodial protrusions distributed at the leading edge and around the perimeter of the migrating cells (Fig. 2c, Ref.[7]). Cell motion is determined by a force balance between the modules and a central cell body (Fig. 3a). The CMS also features a small number of clutches connected directly to the central node, which dampen some of the more abrupt cellular movements and help prevent cases of abnormally high directional persistence. Such central cell-matrix connections are consistent with actual force-bearing perinuclear adhesions found in migrating fibroblasts[34]. Interestingly, perinuclear adhesions are critical for nuclear mechanotransduction, but their possible role in directed cell migration has not been investigated in detail. In the CMS, new modules are nucleated stochastically, module length increases over time via actin polymerization that is simultaneously counteracted by myosin-induced retraction of actin fibers, and modules are removed when they become too short. In addition, total actin and numbers of clutches and motors are kept constant in accordance with the conservation of mass.

In each motor-clutch system, adhesion clutches bind to elastic substrate springs with a constant rate of k_{on}. Connected clutches form a direct mechanical link from the intracellular cytoskeleton to the extracellular substrate – forces are borne from active myosin motors and transmitted by the resulting inward actin flow. The unbinding rate of a connected clutch i, $k_{off,i}$, varies with force F_i according to the Bell model[35]:

$$k_{off,i} = k_{off}^{*} \, exp(F_i / F_b)$$
$$F_i = k_c x_i \qquad \text{(S1)}$$

where k_{off}^{*} is the clutch unbinding rate in the absence of loading, F_b is the characteristic clutch rupture force, and x_i is the elongation of the spring representing the i^{th} connected clutch with a spring constant k_c. The actin filaments are pulled by n_m myosin motors, each capable of exerting a force F_m, and balanced by the traction force F_s, resulting in inward actin flow with the effective actin flow rate (v_m) based on

$$v_m = v_m^* \left(1 - \frac{F_s}{F_{stall}}\right) \quad \text{(S2)}$$

where v_m^* is the unloaded rate, $F_{stall} = n_m F_m$ is the stall force of the ensemble of myosin motors, and the traction force F_s transmitted by all the connected clutches is given by:

$$F_s = \sum_{i=1}^{n_{c,on}} F_i \quad \text{(S3)}$$

in which $n_{c,on}$ is the number of connected clutch bonds. Actin monomers are added to the barbed ends of actin filaments in the cellular protrusions (modules) at a polymerization rate v_p, constrained by the total actin length A_{tot} in the cell according to the relation:

$$v_p = v_p^* (A_{free} / A_{tot}) \quad \text{(S4)}$$

where A_{free} is the amount of available G-actin and v_p^* is the maximum polymerization rate. Module elongation and retraction both result from this actin polymerization and the actin flow rate (v_m). New modules are nucleated at a nucleation rate k_{mod}, also constrained by actin availability:

$$k_{mod} = k_{mod}^* (A_{free} / A_{tot}) \quad \text{(S5)}$$

where k_{mod}^* is the maximum module nucleation rate. Actin filaments are depolymerized into actin monomers when they pass through the position of the myosin motors. Filaments can also be capped and polymerization arrested by actin capping proteins at a capping rate k_{cap}. Actin filaments, and the corresponding modules, are removed from the simulation when their length falls below l_{min}.

Monte Carlo simulations were conducted using a direct Gillespie Stochastic Simulation Algorithm[36], with each time step determined based on total event rates, including k_{on}, $k_{off,i}$, k_{mod}, and k_{cap}, and the event execution determined based on accumulated event rates. Here we added a maximum cap (100 s^{-1}) on $k_{off,i}$ to increase the simulation efficiency and this modification did not affect the simulation outcomes. The CMS C++ version, described in[37], was modified to account for variations in substrate stiffness (described below), and simulations were conducted in Mesabi computer cluster at the Minnesota Supercomputing Institute (MSI).

After the simulated cells had reached a dynamic steady state (60 min), they were displaced randomly to a 180 μm x 180 μm region (Fig. 3b), and the substrate stiffnesses (k_s) experienced

by the cell body and each protrusion were determined based on their respective y-coordinates (y). The substrate could be either soft (k_{soft}), stiff (k_{stiff}), or between the two extremes [gradients following a normal cumulative distribution function, described by the following error functions (erf)]:

$$k_s = k_{\text{soft}} \qquad -\frac{1}{2}\Delta y_{\text{gradient}} - \Delta y_{\text{plateau}} < y \leq -\frac{1}{2}\Delta y_{\text{gradient}} \tag{S6}$$

$$k_s = k_{\text{soft}} + \frac{1}{2}\left(1 + \text{erf}\left(4y/\Delta y_{\text{gradient}}\right)\right)(k_{\text{stiff}} - k_{\text{soft}}) \qquad -\frac{1}{2}\Delta y_{\text{gradient}} < y \leq \frac{1}{2}\Delta y_{\text{gradient}} \tag{S7}$$

$$k_s = k_{\text{stiff}} \qquad \frac{1}{2}\Delta y_{\text{gradient}} < y \leq \frac{1}{2}\Delta y_{\text{gradient}} + \Delta y_{\text{plateau}} \tag{S8}$$

$$k_s = k_{\text{stiff}} + \frac{1}{2}\left(1 + \text{erf}\left(4\left(y - \Delta y_{\text{gradient}} - \Delta y_{\text{plateau}}\right)/\Delta y_{\text{gradient}}\right)\right)(k_{\text{soft}} - k_{\text{stiff}}) \qquad \frac{1}{2}\Delta y_{\text{gradient}} + \Delta y_{\text{plateau}} < y \leq \frac{3}{2}\Delta y_{\text{gradient}} + \Delta y_{\text{plateau}} \tag{S9}$$

where $\Delta y_{\text{gradient}}$ is the width of a region with stiffness gradient (30 μm) and $\Delta y_{\text{plateau}}$ is the width of a region with constant stiffness (60 μm). This way, the number of cells in both soft and stiff regions was initially the same. In addition, by repeating the same stiffness pattern *ad infinitum*, the finite amount of cells placed in the finite rectangular region was representative of infinite cells placed on an infinite substrate with the same initial distribution of cells between soft and stiff areas. A normal cumulative distribution function was selected due to a finite element model of polyacrylamide, which demonstrated that the effective spring constant around a true stepwise gradient of elastic modulus follows a similar distribution (Supplementary Fig. 7). This was valid regardless of the orientation of the applied traction (soft-to-stiff vs. stiff-to-soft).

Here, we adopted the high-motor-clutch parameter values used previously[7] to describe U-251MG migration on mechanically distinct but isotropic substrates (Supplementary Table 2). Clutch stiffness was further adjusted to 8 pN nm^{-1} to better recapitulate the stiffness-dependence of U-251MG speed *in vitro*[7]. Moreover, the total number of available molecular motors (N_m) was adjusted between 4,000 and 10,000 to evaluate the impact of actomyosin inhibition on the U-251MG stiffness optimum (Fig. 4a–b). During the CMS simulations, cell positions and traction forces were recorded every second. The data collected during the first 60 min were analyzed to ensure that the simulated cells had indeed reached a dynamic steady state. Random motility coefficients (RMC) were calculated as described previously[7]. Briefly, the mean squared displacement, $\langle r^2 \rangle$, was calculated with overlapping time periods Δt = 10 min, 20 min, ..., and plotted as a function of Δt. The first half of the plotted curve was fitted with a straight line (slope = $\langle r^2 \rangle / \Delta t$), and RMC was given by RMC = $\langle r^2 \rangle / 4\Delta t$. Module forces were recorded every 10 min and averaged throughout the simulation to yield the average traction force per module. Custom MATLAB scripts were employed to analyze the change in cell numbers in soft and stiff regions over time, to compare module forces in the soft and stiff parts of the gradients, and to track individual cells over time based on their initial location in soft or graded substrate regions.

On 10–100 pN nm^{-1} gradients, we found that the majority of cells translocated away from stiffer regions and toward soft areas (Fig. 3e–f), which were associated with higher traction forces per module and lower overall migration speed, RMC (Fig. 3c–d). We also tested whether altering the

range of the gradient would affect the durotaxis. On 0.3–3 pN nm^{-1} gradients, the stiffer side was associated with higher traction forces and higher RMC (Supplementary Fig. 9a–b). On these substrates, simulated cells displayed rapid accumulation in the stiffer regions (Supplementary Fig. 9c). Finally, when the gradient was chosen such that there would be no appreciable difference in mean traction forces (100–300 pN nm^{-1}), cells clustered primarily in stiffer regions with lower RMC (Supplementary Fig. 9a–b,d).

In order to track individual cells on stiffness gradients, and to calculate the cells' angular displacements and forward migration indices (FMI), 350 cells were simulated on a continuous 200 µm gradient ranging from 10 to 30 pN nm^{-1}. Cells in a dynamic steady state were positioned randomly within an approximately linear 50 µm region in the middle of the gradient (Fig. 3g) and followed for an additional 14 hours of simulation time. FMIs, defined as Δy divided by the total track length (accumulated distance), and where positive values denote migration toward increasing stiffness, indicated that the cells moved preferentially toward the softer side of the stiffness gradient – in accordance with their predicted stiffness optimum (Fig. 3h–i).

Supplementary Note 3: Modeling axonal pathfinding and mechanosensitive steering of growth cones

Axonal growth cones (GCs) (Supplementary Fig. 10a) can turn or contract in response to substrate stiffness gradients[38,39] by controlling the dynamics of adhesions, filopodial remodeling, and active contraction[40]. To establish whether motor-clutch dynamics could explain the mechanosensitive turning of neuronal GCs[38], akin to the negative durotaxis exhibited by the U-251MG glioblastoma cells, we modified the CMS to model an individual GC on a functionally graded substrate. A group of i filopodia, each modeled as a single molecular clutch module (Supplementary Fig. 10b), were attached to a GC central domain. Each module was allocated n_i molecular clutches (linear springs of stiffness k_c) and n_i corresponding substrate clutches (linear springs of stiffness $k_{s,i}$). Substrate clutches were distributed randomly, and had values $k_{s,1} \leq k_{s,i} \leq k_{s,2}$ that varied linearly with position along the gradient.

Monte Carlo simulations were conducted to evaluate filopodial and GC dynamics over time. We modeled a GC as having 21 potential growth sites for filopodia, chosen from a uniform orientation distribution between –π/2 and π/2, relative to the direction of the 'axon'. New protrusions with an initial length l_{in} and width l_{wid}, dictating the effective clutch-ligand binding area, were added into the simulation at a rate k_{mod} and assigned n_m myosin motors; note that we used an actin filament in the schematic diagram (Supplementary Fig. 11a) to represent the filament bundle in the filopodium. The adhesion and substrate clutches under each filament then evolved according to the clutch binding and unbinding dynamics described above. Unlike the cellular level CMS, our modified model assumes a relatively stable pool of actin monomer in the GC. Thus, the actin polymerization rate v_p remained constant during each simulation. See Supplementary Table 3 for parameter details.

First, we investigated whether the dozens of filopodia within a GC might enable mechanically directed growth by evaluating the response of an individual 8 μm filopodium to a linear stiffness gradient of 0.01 to 100 pN nm^{-1} (Supplementary Fig. 10b). The filopodium was placed on a 10 μm x 10 μm square substrate and oriented at an angle $0 \leq \theta \leq \pi/2$ relative to the gradient (Supplementary Fig. 10c). When the filopodium length was fixed, simply increasing the orientation between the filopodium and the gradient was sufficient to significantly increase traction force generation (Supplementary Fig. 10d). Conversely, when the orientation was fixed at π/2, i.e. perpendicular to the gradient, we found that both traction force and the number of engaged clutches increased linearly with filopodium length (Supplementary Fig. 10d).

Next, we investigated the impact of different stiffness gradients for traction force generation using a fixed filopodium length (8 μm) and orientation (0). Maximal traction forces resulted from the filopodium sensing a soft region, in the range of 0.01 to 0.1 pN nm^{-1}. The higher end of the

stiffness gradient proved significantly less important for the overall traction (Supplementary Fig. 10e). This result demonstrates that a filopodium can generate comparatively high forces even if only a part of it is located on softer substrate. Thus, high traction force generation by individual filopodia is favored at a low optimal stiffness and forces drastically drop on stiffer matrices.

Higher traction forces are often accompanied by a decrease in actin retrograde flow, as myosin-borne forces are transmitted to the ECM instead of freely displacing actin. Regardless of filopodia orientation, actin in GCs flows toward the structure's center, and much like traction forces, actin flow rates can also differ for different types of neurons[41]. We therefore investigated how both the speed and direction of actin flow relative to the stiffness gradient affect the dynamics of single filopodia. By studying filopodia oriented at their growing end with either the stiffer or more compliant end of a stiffness gradient (Supplementary Fig. 10f), we found that orientation toward the compliant end of the substrate (and hence actin retrograde flow toward the stiff end of the substrate) led to increased extension rates and decreased retraction rates (Supplementary Fig. 10g). In all cases, the overall growth rate of filopodia was a trade-off between growth at the constant actin polymerization rate v_p, and shortening at the actin flow rate v_m, which varied almost linearly with substrate stiffness (Supplementary Fig. 10h). For an intermediate polymerization rate of v_p = 120 nm s^{-1}, orientation affected filopodia growth rate by a factor of two (Supplementary Fig. 10h). Together, these results provide a mechanism by which individual filopodia can exert more traction and elongate faster on softer substrates.

We then investigated whether these changes in filopodial dynamics could contribute to GC steering on stiffness gradients. First, we evaluated the degree of GC turning on one type of stiffness gradient ($k_{s,1}$ = 0.01 pN nm^{-1} and $k_{s,2}$ = 100 pN nm^{-1}) by studying an initially semicircular GC with 21 uniformly distributed filopodia (Supplementary Fig. 11a). Within 15 seconds of simulation, the filopodia pointing toward the compliant end of the substrate outgrew the rest, resulting in an effective turning of the GC (Supplementary Fig. 11a). As expected from the previous results, filopodia in the softer regions of the gradient were longer and generated higher traction forces (Supplementary Fig. 11b).

To investigate the effect of different stiffness gradients on GC turning in detail, we repeated our simulations over a broad range of possible substrate stiffnesses, with $k_{s,left}$ and $k_{s,right}$ varying from 0.01 to 100 pN nm^{-1}. To quantify the degree of turning, we defined a parameter $\Lambda = \bar{l}_{left} / \bar{l}_{right}$, which represents the degree to which the GC has turned left. Here, $\bar{l}_{left}$ and $\bar{l}_{right}$ are the average lengths of filopodia in the left-hand and right-hand sides of the GC after 100 seconds of simulation, respectively. In addition to developing polarity through turning, the GC could enlarge, with all filopodia elongating as compared to their initial length, or retract (Supplementary Fig. 11c). Enlarged GCs appeared on very compliant substrates (red section, $k_{s,left}$ and $k_{s,right}$ on the order of 0.01 to 0.1 pN nm^{-1}) with a negligible stiffness gradient, and

retractile GCs appeared on higher stiffnesses, independent of the actual strength of the gradient (green section, $k_{s,left}$ and $k_{s,right}$ on the order of 1 to 100 pN nm^{-1}). Finally, polarized GCs appeared on compliant substrates with a moderate or high stiffness gradient ($k_{s,left}$ on the order of 0.01 to 0.1 pN nm^{-1}, >1 pN/nm/20 μm). A phase diagram for GC turning illustrates how the structure can either remain straight or turn to the more compliant side (Supplementary Fig. 11d), and reveals that a stronger gradient may also promote GC turning, unless the range of the gradient as a whole is significantly stiffer than the optimal stiffness range for individual filopodia (Supplementary Fig. 11e). Thus, the motor-clutch model can recapitulate mechanosensitive GC steering toward softer matrix *in silico*.

Supplementary Table 1. Relative acrylamide and bis-acrylamide concentrations and corresponding Young's moduli for homogeneous (constant modulus) hydrogels

Final acrylamide %	Final bis-acrylamide %	Volume of (40%) AA stock, µl	Volume of (2%) bis-AA stock, µl	PBS, µl	~Young's modulus, kPa*
5.4	0.04	63	10	397	0.5
5.7	0.08	63	17.5	365	2
7.5	0.2	94	50	356	9.6
12	0.2	150	50	300	22
18	0.4	225	100	175	60

*Values obtained using atomic force microscopy, see Ref.[1]

Supplementary Table 2. Parameters for the cellular level CMS

Parameter	Symbol	Value	Ref.
Total number of myosin motors	N_m	(4,000–)10,000	[7], adjusted
Total number of clutches	N_c	7,500	[7]
Maximum total actin length	A_{tot}	100 µm	[7]
Maximum actin polymerization rate	v_p^*	200 nm/s	[7]
Maximum module nucleation rate	k_{mod}^*	1 s^{-1}	[7]
Module capping rate	k_{cap}	0.001 s^{-1}	[7]
Initial module length	l_{in}	5 µm	[7]
Minimum module length	l_{min}	0.1 µm	[7]
Cell spring constant	k_{cell}	10,000 pN/nm	[7]
Number of cell body clutches	$n_{c,cell}$	10	[7]
Substrate spring constant	k_s	0.3–300 pN/nm	Adjusted
Maximum number of module motors	n_m^*	1,000	[7]
Myosin motor stall force	F_m	2 pN	[7]
Unloaded actin flow rate	v_m^*	120 nm/s	[7]
Maximum number of module clutches	n_c^*	750	[7]
Clutch on-rate	k_{on}	1 s^{-1}	[7]
Unloaded clutch off-rate	k_{off}^*	0.1 s^{-1}	[7]
Clutch spring constant	k_c	8 pN/nm	Adjusted
Characteristic clutch rupture force	F_b	2 pN	[7]

Supplementary Table 3. Parameters for the filopodia/GC model

Parameter	Symbol	Value	Ref.
Actin polymerization rate	v_p	90–130 nm/s	[42], adjusted
Module nucleation rate	k_{mod}	1 s^{-1}	[7]
Initial filopodium length	l_{in}	3 μm	Adapted from [7]
Minimum filopodium length	l_{min}	0.1 μm	Adapted from [7]
Filopodium width for ligand binding	l_{wid}	0.2 μm	[43]
Substrate spring constant (soft region)	$k_{s,1}$	10^{-2}–10^{2} pN/nm	Adjusted
Substrate spring constant (stiff region)	$k_{s,2}$	10^{-2}–10^{2} pN/nm	Adjusted
Initial number of module motors	n_m	50	[5]
Myosin motor stall force	F_m	2 pN	[5]
Unloaded actin flow rate	v_m^*	120 nm/s	[5]
Initial number of module clutches	n_c	50	[5]
Clutch on-rate	k_{on}	0.3 s^{-1}	[5]
Unloaded clutch off-rate	k_{off}^*	0.1 s^{-1}	[5]
Clutch spring constant	k_c	1 pN/nm	[5]
Characteristic clutch rupture force	F_b	2 pN	[5]

Captions for Supplementary Videos 1–3

Supplementary Video 1. Evolution of U-251MG glioblastoma cell distribution on photoresponsive stiffness gradient hydrogels over time. Blue overlay in the middle denotes a softer, UV-irradiated region. Vertical and horizontal lines are out-of-focus markings on the underlying glass. Scale bar, 200 μm.

Supplementary Video 2. Migration of individual U-251MG cells on photoresponsive stiffness gradient hydrogels. (Top) Phase-contrast data showing migrating cells over the span of 24 hours. Scale bar, 100 μm. (Bottom) Tracks corresponding to the cells in the top panel. Softer, UV-irradiated hydrogel is marked with gray color.

Supplementary Video 3. DMSO- and H-1152-treated U-251MG cells migrating on stiffness gradients. Phase-contrast movies of migrating glioma cells treated with 0.1% DMSO (left) or 5 μM H-1152 (right) for 10 hours. The cells are on continuous 0.5-22 kPa stiffness gradients, in the >10 kPa region (with substrate stiffness increasing toward the top). Scale bar, 50 μm.

Supplementary References

1. Barber-Pérez, N. *et al.* Mechano-responsiveness of fibrillar adhesions on stiffness-gradient gels. *J. Cell Sci.* 133, (2020).
2. Chan, C. E. & Odde, D. J. Traction Dynamics of Filopodia on Compliant Substrates. *Science* 322, 1687–1691 (2008).
3. Elosegui-Artola, A. *et al.* Mechanical regulation of a molecular clutch defines force transmission and transduction in response to matrix rigidity. *Nat. Cell Biol.* 18, 540–548 (2016).
4. Bangasser, B. L. & Odde, D. J. Master equation-based analysis of a motor-clutch model for cell traction force. *Cell. Mol. Bioeng.* 6, 449–459 (2013).
5. Bangasser, B. L., Rosenfeld, S. S. & Odde, D. J. Determinants of maximal force transmission in a motor-clutch model of cell traction in a compliant microenvironment. *Biophys. J.* 105, 581–592 (2013).
6. Cheng, B. *et al.* An Integrated Stochastic Model of Matrix-Stiffness-Dependent Filopodial Dynamics. *Biophys. J.* 111, 2051–2061 (2016).
7. Bangasser, B. L. *et al.* Shifting the optimal stiffness for cell migration. *Nat. Commun.* 8, 1–10 (2017).
8. Lerche, M. *et al.* Integrin Binding Dynamics Modulate Ligand-Specific Mechanosensing in Mammary Gland Fibroblasts. *iScience* 23, 100907 (2020).
9. Yeung, T. *et al.* Effects of substrate stiffness on cell morphology, cytoskeletal structure, and adhesion. *Cell Motil. Cytoskeleton* 60, 24–34 (2005).
10. Caliari, S. R. & Burdick, J. A. A practical guide to hydrogels for cell culture. *Nat. Methods* 13, 405–414 (2016).
11. Hartman, C. D., Isenberg, B. C., Chua, S. G. & Wong, J. Y. Vascular smooth muscle cell durotaxis depends on extracellular matrix composition. *Proc. Natl. Acad. Sci.* 113, 11190–11195 (2016).
12. Hadden, W. J. *et al.* Stem cell migration and mechanotransduction on linear stiffness gradient hydrogels. *Proc. Natl. Acad. Sci.* 114, 5647–5652 (2017).
13. Kim, T. H. *et al.* Creating stiffness gradient polyvinyl alcohol hydrogel using a simple gradual freezing-thawing method to investigate stem cell differentiation behaviors. *Biomaterials* 40, 51–60 (2015).
14. Jiang, F. X., Yurke, B., Schloss, R. S., Firestein, B. L. & Langrana, N. A. Effect of dynamic stiffness of the substrates on neurite outgrowth by using a DNA-crosslinked hydrogel. *Tissue Eng. Part A* 16, 1873–1889 (2010).
15. Khetan, S. *et al.* Degradation-mediated cellular traction directs stem cell fate in covalently crosslinked three-dimensional hydrogels. *Nat. Mater.* 12, 458–465 (2013).
16. Martinez, J. S., Lehaf, A. M., Schlenoff, J. B. & Keller, T. C. S. Cell Durotaxis on Polyelectrolyte Multilayers with Photogenerated Gradients of Modulus. *Biomacromolecules* 14, 1311–1320 (2013).
17. Rosales, A. M., Vega, S. L., DelRio, F. W., Burdick, J. A. & Anseth, K. S. Hydrogels with Reversible Mechanics to Probe Dynamic Cell Microenvironments. *Angew. Chem. Int. Ed Engl.* 56, 12132–12136 (2017).
18. Mosiewicz, K. A., Kolb, L., van der Vlies, A. J. & Lutolf, M. P. Microscale patterning of hydrogel stiffness through light-triggered uncaging of thiols. *Biomater. Sci.* 2, 1640–1651 (2014).
19. Sunyer, R., Jin, A. J., Nossal, R. & Sackett, D. L. Fabrication of hydrogels with steep stiffness gradients for studying cell mechanical response. *PloS One* 7, e46107 (2012).
20. Mahmoodi, M. M. *et al.* Nitrodibenzofuran: A One- and Two-Photon Sensitive Protecting Group That Is Superior to Brominated Hydroxycoumarin for Thiol Caging in Peptides. *J. Am. Chem. Soc.* 138, 5848–5859 (2016).
21. Wieboldt, R. *et al.* Photolabile precursors of glutamate: synthesis, photochemical properties, and activation of glutamate receptors on a microsecond time scale. *Proc. Natl. Acad. Sci. U. S. A.* 91, 8752–8756 (1994).
22. Griffin, D. R., Patterson, J. T. & Kasko, A. M. Photodegradation as a mechanism for controlled drug delivery. *Biotechnol. Bioeng.* 107, 1012–1019 (2010).

23. Sanford, M. S., Charles, P. T., Commisso, S. M., Roberts, J. C. & Conrad, D. W. Photoactivatable Cross-Linked Polyacrylamide for the Site-Selective Immobilization of Antigens and Antibodies. *Chem. Mater.* 10, 1510–1520 (1998).
24. Yan, B., Boyer, J.-C., Habault, D., Branda, N. R. & Zhao, Y. Near infrared light triggered release of biomacromolecules from hydrogels loaded with upconversion nanoparticles. *J. Am. Chem. Soc.* 134, 16558–16561 (2012).
25. Badeau, B. A., Comerford, M. P., Arakawa, C. K., Shadish, J. A. & DeForest, C. A. Engineered modular biomaterial logic gates for environmentally triggered therapeutic delivery. *Nat. Chem.* 10, 251–258 (2018).
26. DeForest, C. A. & Tirrell, D. A. A photoreversible protein-patterning approach for guiding stem cell fate in three-dimensional gels. *Nat. Mater.* 14, 523–531 (2015).
27. Kloxin, A. M., Kasko, A. M., Salinas, C. N. & Anseth, K. S. Photodegradable hydrogels for dynamic tuning of physical and chemical properties. *Science* 324, 59–63 (2009).
28. Wong, D. Y., Griffin, D. R., Reed, J. & Kasko, A. M. Photodegradable Hydrogels to Generate Positive and Negative Features over Multiple Length Scales. *Macromolecules* 43, 2824–2831 (2010).
29. Klinger, D. & Landfester, K. Photo-sensitive PMMA microgels: light-triggered swelling and degradation. *Soft Matter* 7, 1426–1440 (2011).
30. Ramanan, V. V. *et al.* Photocleavable side groups to spatially alter hydrogel properties and cellular interactions. *J. Mater. Chem.* 20, 8920–8926 (2010).
31. Frey, M. T. & Wang, Y.-L. A photo-modulatable material for probing cellular responses to substrate rigidity. *Soft Matter* 5, 1918–1924 (2009).
32. Wang, Y. L. & Pelham, R. J. Preparation of a flexible, porous polyacrylamide substrate for mechanical studies of cultured cells. *Methods Enzymol.* 298, 489–496 (1998).
33. Denisin, A. K. & Pruitt, B. L. Tuning the Range of Polyacrylamide Gel Stiffness for Mechanobiology Applications. *ACS Appl. Mater. Interfaces* 8, 21893–21902 (2016).
34. Shiu, J.-Y., Aires, L., Lin, Z. & Vogel, V. Nanopillar force measurements reveal actin-cap-mediated YAP mechanotransduction. *Nat. Cell Biol.* 20, 262–271 (2018).
35. Bell, G. I. Models for the specific adhesion of cells to cells. *Science* 200, 618–627 (1978).
36. Gillespie, D. T. Exact stochastic simulation of coupled chemical reactions. *J. Phys. Chem.* 81, 2340–2361 (1977).
37. Hou, J. C. *et al.* Modeling distributed forces within cell adhesions of varying size on continuous substrates. *Cytoskeleton* 76, 571–585 (2019).
38. Koser, D. E. *et al.* Mechanosensing is critical for axon growth in the developing brain. *Nat. Neurosci.* 19, 1592–1598 (2016).
39. Franze, K. *et al.* Neurite branch retraction is caused by a threshold-dependent mechanical impact. *Biophys. J.* 97, 1883–1890 (2009).
40. Betz, T., Koch, D., Lu, Y.-B., Franze, K. & Käs, J. A. Growth cones as soft and weak force generators. *Proc. Natl. Acad. Sci.* 108, 13420–13425 (2011).
41. Koch, D., Rosoff, W. J., Jiang, J., Geller, H. M. & Urbach, J. S. Strength in the Periphery: Growth Cone Biomechanics and Substrate Rigidity Response in Peripheral and Central Nervous System Neurons. *Biophys. J.* 102, 452–460 (2012).
42. Gomez, T. M. & Letourneau, P. C. Actin Dynamics in Growth Cone Motility and Navigation. *J. Neurochem.* 129, 221 (2014).
43. Atilgan, E., Wirtz, D. & Sun, S. X. Mechanics and dynamics of actin-driven thin membrane protrusions. *Biophys. J.* 90, 65–76 (2006).

Supplementary Data files related to the Supplementary Figures

- Supplementary Data 1: statistical source data for Supplementary Fig. 1
- Supplementary Data 2: statistical source data for Supplementary Fig. 2
- Supplementary Data 3: statistical source data for Supplementary Fig. 3
- Supplementary Data 4: statistical source data for Supplementary Fig. 5
- Supplementary Data 5: statistical source data for Supplementary Fig. 6
- Supplementary Data 6: statistical source data for Supplementary Fig. 7
- Supplementary Data 7: statistical source data for Supplementary Fig. 8
- Supplementary Data 8: statistical source data for Supplementary Fig. 9
- Supplementary Data 9: statistical source data for Supplementary Fig. 10
- Supplementary Data 10: statistical source data for Supplementary Fig. 11
- Supplementary Data 11: statistical source data for Supplementary Fig. 12
- Supplementary Data 12: statistical source data for Supplementary Fig. 13
- Supplementary Data 13: statistical source data for Supplementary Fig. 14